Journal of Pharmaceutical Analysis 14 (2024) 100969

Contents lists available at ScienceDirect

Journal of Pharmaceutical Analysis

journal homepage: www.elsevier.com/locate/jpa

Original article

CA IX-targeted Ag_2S quantum dots bioprobe for NIR-II imaging-guided hypoxia tumor chemo-photothermal therapy

Xinyue Cui [a, b, 1], Zhuang Hu [a, b, 1], Ruihan Li [a, b], Peng Jiang [a, b], Yongchang Wei [a, **], Zilin Chen [a, b, *]

[a] Department of Radiation and Medical Oncology, Zhongnan Hospital of Wuhan University and School of Pharmaceutical Sciences, Wuhan University, Wuhan, 430071, China
[b] Key Laboratory of Combinatorial Biosynthesis and Drug Discovery, Ministry of Education, Hubei Province Engineering and Technology Research Center for Fluorinated Pharmaceuticals, Wuhan, 430071, China

ARTICLE INFO

Article history:
Received 20 September 2023
Received in revised form
5 February 2024
Accepted 20 March 2024
Available online 22 March 2024

Keywords:
CA IX-targeted
Hypoxia tumor combination therapy
NIR-II imaging
Photothermal effect

ABSTRACT

Hypoxia is the common characteristic of almost all solid tumors, which prevents therapeutic drugs from reaching the tumors. Therefore, the development of new targeted agents for the accurate diagnosis of hypoxia tumors is widely concerned. As carbonic anhydrase IX (CA IX) is abundantly distributed on the hypoxia tumor cells, it is considered as a potential tumor biomarker. 4-(2-Aminoethyl)benzenesulfonamide (ABS) as a CA IX inhibitor has inherent inhibitory activity and good targeting effect. In this study, Ag_2S quantum dots (QDs) were used as the carrier to prepare a novel diagnostic and therapeutic bioprobe (Ag_2S@polyethylene glycol (PEG)-ABS) through ligand exchange and amide condensation reaction. Ag_2S@PEG-ABS can selectively target tumors by surface-modified ABS and achieve accurate tumor imaging by the near infrared-II (NIR-II) fluorescence characteristics of Ag_2S QDs. PEG modification of Ag_2S QDs greatly improves its water solubility and stability, and therefore achieves high photothermal stability and high photothermal conversion efficiency (PCE) of 45.17%. Under laser irradiation, Ag_2S@PEG-ABS has powerful photothermal and inherent antitumor combinations on colon cancer cells (CT-26) *in vitro*. It also has been proved that Ag_2S@PEG-ABS can realize the effective treatment of hypoxia tumors *in vivo* and show good biocompatibility. Therefore, it is a new efficient integrated platform for the diagnosis and treatment of hypoxia tumors.

1. Introduction

Cancer has emerged as one of the leading causes of death and a major barrier to extending human life expectancy in recent years [1]. According to the Global Cancer Statistics 2020, cancer is the primary or secondary cause of death in 112 countries, and one in five people worldwide will develop cancer in their lifetime, which seriously affects how long patients can live or a good quality of life. Among all cancers, colon cancer has the third highest incidence rate of 10% and the second highest mortality rate of 9.4% [2]. Hypoxia is used by cancer cells as a means of defense against immune system attack or therapeutic interventions, leading to immunological evasion and treatment resistance. The imbalance and undersupply of oxygen demand in cancer cells are due to dysfunction of tumor vessels [3,4]. Nearly all solid tumors exhibit features of hypoxia in their intratumoral regions, often known as the tumor microenvironment [5]. Hypoxia upregulates many genes by hypoxia-inducible factor-1 alpha (HIF-1α), including two carbonic anhydrases, carbonic anhydrase IX (CA IX) and CA XII. Among them, CA IX is more relevant to tumors. CA IX is a transmembrane enzyme that catalyzes the retrograde conversion of carbon dioxide into carbonic acid [6]. CA IX can decrease extracellular pH and increase intracellular pH. Relatively high intracellular pH is conducive to the survival and proliferation of tumor cells, while extracellular acidic environment is conducive to tumor migration and adhesion, which is the cause of late metastasis and deterioration of most tumors. The fact that solid tumors specifically overexpress CA IX under hypoxia conditions and has limited expression in normal tissues makes it an attractive diagnostic and therapeutic marker [7]. 4-(2-Aminoethyl)benzenesulfonamide (ABS) is a CA IX inhibitor with

* Corresponding author. Department of Radiation and Medical Oncology, Zhongnan Hospital of Wuhan University and School of Pharmaceutical Sciences, Wuhan University, Wuhan, 430071, China.
** Corresponding author.
E-mail addresses: chenzl@whu.edu.cn (Z. Chen), weiyongchang@whu.edu.cn (Y. Wei).
[1] Both authors contributed equally to this work.

https://doi.org/10.1016/j.jpha.2024.100969

strong targeting specificity and binding affinity [8]. Therefore, the development of ABS-based CA IX-targeting diagnosis and treatment probes are becoming increasingly important. According to recent studies, CA IX is overexpressed in colon cancer, cervical cancer, breast cancer, and non-small cell renal cancer [9–11]. A novel small-molecule drug combination was recently created by Neri and co-workers [12] using a high-affinity ligand of CA IX. The combination of the new small-molecule drug and L19-IL2 was also able to eradicate 100% of tumor in immunocompetent mice carrying subcutaneously transplanted CT-26 colon cancer cells fully expressing CA IX. Therefore, CA IX is a crucial target for the detection and treatment of hypoxia tumors such as colon cancer.

Currently, clinical diagnosis imaging methods for tumors include magnetic resonance imaging (MRI), positron emission tomography (PET), computed tomography (CT), etc., but these technologies generally have problems such as high equipment cost, ionizing radiation risk, and poor spatial and temporal resolution [13]. Studies showed that compared with the visible region of 400–700 nm and the near infrared-I (NIR-I) of 700–900 nm, *in vivo* fluorescence imaging of the NIR-II of 1000–1700 nm has unique advantages such as reduced absorption, decreased fluorescence index of tissue itself, and reduced photon scattering loss [14–16]. This can significantly improve the spatial resolution, signal-to-noise ratio, and penetration depth of NIR-II imaging, which is very advantageous for high-performance in tumor imaging [17–20]. At present, inorganic nanoparticles based on quantum dots (QDs) are widely applied to *in vivo* imaging and disease diagnosis, showing excellent results. Traditional NIR QDs (such as PbSe [21] and CdHgTe [22]) are restricted in their applications in biological systems because they contain toxic heavy metal ions. Good biocompatibility is a necessary condition for its deep application in biology. Silver chalcogenide QDs are appropriate for use in the biological and biomedical fields because of their low cytotoxicity. Silver sulfide (Ag_2S), silver selenide (Ag_2Se), and silver telluride (Ag_2Te) are the three primary forms of silver chalcogenide QDs. Compared with Ag_2S QDs, Ag_2Te QDs and Ag_2Se QDs perform relatively poorly as nanocarriers and bioimaging probes. At present, the majority of Ag_2X QDs focuses on the synthesis and application of Ag_2S QDs [23]. Ag_2S QDs as a kind of colloidal semiconductor nanocrystals have adjustable size, high fluorescence brightness, good photostability, and high photothermal conversion efficiency (PCE) under NIR-II [24]. In addition, Ag_2S QDs do not contain heavy metals and have a high specific surface area, which can avoid the toxicity caused by heavy metals, and is conducive to further modification and *in vivo* application research. A single precursor source was used to create NIR fluorescent Ag_2S QDs (1058 nm emission) according to a 2010 report by Wang and co-workers [25]. The authors then proved the biocompatibility and bioimaging capabilities of this NIR Ag_2S QDs. Recently, the application of Ag_2S QDs in tumor imaging diagnosis [26,27], chemotherapy [28], sonodynamic therapy [29], and photothermal therapy [30] has been widely explored. However, the colloidal stability of Ag_2S QDs is poor in physiological environment, which seriously limits its practical application in cancer diagnosis and treatment [31–34].

PEGylation of drugs is the gold standard for the treatment of cancer and other diseases in the pharmaceutical industry [35], which has excellent water solubility and flexibility. To a certain extent, PEGylation can prevent the recognition of opsonin *in vivo* and the binding of plasma proteins, so help nanomaterials escape from the reticuloendothelial system [36]. Therefore, the use of polyethylene glycol (PEG) for surface modification can increase stability and make nano-preparations more biocompatible, and reduce systemic toxicity.

As a nanomaterial with strong NIR absorption capacity, Ag_2S QDs also show enormous potential for the photothermal cancer treatment. Photothermal therapy (PTT) refers to a treatment that uses a photosensitizer to generate heat from light, which causes cancer cells to be thermally ablationed and ultimately die. PTT has achieved noninvasive and effective eradication in a wide range of malignancies [37,38]. By modifying QDs with targeted molecules, tumors can be precisely ablated, and at the same time the damage to surrounding healthy tissue can be minimized [39–41]. Liu and co-workers [42] reported the successful synthesis of genetically engineered peptide RGDPC$_{10}$A-encapsulated Ag_2S QDs (CPCC–Ag_2S QDs). CPCC-Ag_2S QDs exhibit excellent fluorescence imaging and photothermal performance in the NIR-II biological window. The tumor site temperature of tumor-bearing mice injected with CPCC-Ag_2S QDs was stable at 61.2 °C after 10 min, and tumor cells were effectively killed by hyperthermia. However, when inorganic nanoparticles enter the human circulatory system and target tumors, they often encounter interference from biological barriers and damage from the potential toxicity of heavy metals [43,44]. Thus, biological barriers and toxicity of materials limit further clinical applications.

In recent years, our group has concentrated on the imaging and treatment of hypoxic tumors in the near-infrared region [45–50]. Herein, a NIR-II bioprobe Ag_2S@PEG-ABS with PEG modified passive targeting photothermal agent Ag_2S QDs and active targeting agent ABS was constructed and developed for inhibitor anti-tumor and photothermal synergistic therapy. Ag_2S@PEG was prepared by modifying PEG on the surface of Ag_2S QDs. Ag_2S@PEG was further modified by ABS to effectively target CA IX, which is overexpressed in hypoxia tumors such as colon cancer. The intense fluorescence of Ag_2S QDs at 1135 nm in the NIR-II can achieve the accurate detection of hypoxia tumors, and the fluorescence intensity ratio of tumor to normal tissue can reach more than 10, which is of highly significance for the diagnosis of hypoxia tumors. The half maximal inhibitory concentration (IC_{50}) of ABS was 2.8 ± 0.4 mM, indicating that ABS had a certain anti-tumor effect. The IC_{50} of the Ag_2S@PEG-ABS was 263.9 ± 7.1 μg/mL. This is due to the excellent photothermal performance of the bioprobe with a PCE of 45.17%. The *in vivo* results also showed that tumor ablation was achieved by combination of inhibitors and photothermal therapy, which effectively inhibited tumor growth and metastasis. On the whole, the bioprobe Ag_2S@PEG-ABS has the advantages of simple preparation, good biocompatibility, and high PCE, which can be used for early diagnosis and treatment of hypoxia tumors.

2. Experimental

2.1. Materials

ABS was obtained from Bide Pharmatech Co., Ltd. (Shanghai, China). Silver nitrate, 3-mercaptopropionic acid (3-MPA), and ethylene glycol were purchased from Shanghai Zhanyun Chemical Co., Ltd. (Shanghai, China), Macklin (Shanghai, China), and Sinopharm Chemical Reagent Co., Ltd. (Shanghai, China), respectively. *N*-hydroxysuccinimide (NHS) and *N*-(3-dimethylaminopropyl)-*N*′-ethylcarbodiimide hydrochloride (EDC) were bought from Sigma-Aldrich (Saint Louis, MO, USA). HS-PEG-COOH (molecular weight (MW) = 1000) was purchased from Ponsure Biological Co., Ltd. (Shanghai, China). All other materials, including solvents, were of the reagent or high performance liquid chromatography (HPLC) grade.

2.2. Synthesis of Ag_2S@PEG-ABS

2.2.1. Synthesis of Ag_2S QDs

There was a reference to earlier work for the manufacture of water-soluble Ag_2S QDs [51]. Briefly, 10 mL of ethylene glycol was introduced in a 25 mL three-necked round-bottomed flask and

degassed for 30 min. After that, ethylene glycol was heated to 110 °C and then 8.45 mg of $AgNO_3$ (0.05 mmol) and 100 μL of 3-MPA were added to the reaction system. The mixture began to turn milky white, yellow, brown, and dark brown following the temperature rised to 150 °C. After 2 h vigorous mechanical stirring, the reaction is stopped. Finally, the reaction products were collected by washed three times with a 30 kDa ultrafiltration centrifuge tube (2,500 rpm, 60 min), and the Ag_2S QDs were stored in a refrigerator at 4 °C for subsequent synthesis and property determination.

2.2.2. Synthesis of Ag_2S@PEG-ABS

Ag_2S@PEG-ABS was obtained by the following reaction (Fig. S1). 20 μmol HS-PEG-COOH (MW = 1000) was added to the Ag_2S QDs aqueous solution (5 mL, 10 mM Ag^+) to react under a nitrogen atmosphere for 12 h. Ag_2S@PEG was then washed three times by centrifugal. Then, the Ag_2S@PEG was mixed with 50 μmol EDC and 100 μmol NHS to activate the carboxyl group of the PEG for 60 min. After that, 50 μmol ABS was added to the aforementioned combination, and the reaction proceeded for 12 h. Finally, the Ag_2S@PEG-ABS was gathered using an ultrafiltration centrifuge tube (2,500 rpm, 60 min) and the superfluous reactants were discarded. The product was stored in a refrigerator at 4 °C for subsequent property determination and application.

2.3. The structural characterization

The transmission electron microscopy (TEM) was performed on JEM-F200 (JEOL, Tokyo, Japan). On the Malvern Zetasizer Nano ZS90 (Malvern, Malvern, UK), zeta potential values and hydrodynamic diameters were obtained. Fourier transform infrared (FT-IR) spectroscopy were detected by Thermo Nicolet NEXUS 470 (Thermo Fisher Scientific Inc., Waltham, MA, USA). The fluorescence spectra were measured by FLS-1000 fluorescence spectrophotometer (Edinburgh Instruments, Edinburgh, UK). The ultraviolet (UV) absorption spectrum was detected by an UV-3600 spectrophotometer (Shimadzu Corporation, Kyoto, Japan).

2.4. Photothermal performance

To evaluate the photothermal properties of the bioprobe prepared, different concentrations were dispersed in water and exposed to an 808 nm (1.5 W/cm^2) using a diode laser (Hi-Tech Optoelectronics Co., Ltd., Beijing, China). Infrared thermal imaging camera was used to measure the temperature change of the bioprobe under irradiation, and calculate PCE (η) according to Eq. 1:

$$\eta = \frac{hS \times (T_{max} - T_{surr}) - Q_0}{I \times \left(1 - 10^{-A_{808}}\right)} \quad \text{Eq. (1)}$$

where h and S represent the heat transfer coefficient of the solvent and the surface area of the cuvette, respectively. T_{max} and T_{surr} stand for the maximum temperature of the solvent during the irradiation period and the initial temperature. Q_0 is measured by the heat absorbed by the solvent under irradiation. I refer to the power density, and A_{808} is the absorbance value of the bioprobe at 808 nm, which can be measured by UV-visible (vis)-NIR spectrophotometer. The calculation of hS can be obtained by Eq. 2:

$$hS = \frac{mC}{\tau} \quad \text{Eq. (2)}$$

m means that mass of the solution which is equal to 1.0 g, C stands for the solution specific heat capacity is equal to 4.2 J/g, and τ is the time constant associated with the cooling period and can be obtained by Eq. 3:

$$\tau = \frac{-t}{\ln\theta} \quad \text{Eq. (3)}$$

where $\theta = \Delta T/\Delta T_{max}$, the fitting curve was obtained by fitting $-\ln\theta$ with the time change during the cooling period, and τ was calculated from the slope of the obtained curve. Finally, the PCE of Ag_2S@PEG-ABS can be calculated according to Eq. 1.

2.5. Photothermal imaging

Different concentrations of Ag_2S@PEG-ABS solutions (0, 0.1, 0.2, 0.4, and 1 mg/mL) were taken and placed in a quartz dish and irradiated using an 808 nm laser (1.5 W/cm^2) for 10 min, and an infrared camera captured the images and recorded temperature changes. Then the concentration of Ag_2S@PEG-ABS was fixed at 0.4 mg/mL and the laser power (1, 1.5, and 2 W/cm^2) was changed to test the effect of power on the photothermal performance. To explore the photothermal stability of the bioprobe, the temperature was increased and then cooled for three cycles. For *in vivo* photothermal imaging, Ag_2S QDs and Ag_2S@PEG-ABS were injected via the tail vein of anesthetized CT-26 tumor-bearing mice. After 6 h, the temperature of the tumor was detected with an infrared thermal imager under the laser (808 nm, 1.5 W/cm^2, 5 min) irradiation.

2.6. Cell culture

Mouse colon cancer cell lines CT-26 was purchased from the Cell Storage Center of Wuhan University. The mouse colon cancer cell lines CT-26 were cultured in Roswell Park Memorial Institute (RPMI) 1640 (10% fetal bovine serum (FBS) and 1% Penicillin-Streptomycin-Amphotericin B Solution (100×)). In normoxia conditions, the cells were cultivated in a humidified 5% CO_2 incubator at 37 °C. In hypoxia conditions, the cells were cultivated in a hypoxia incubator at 37 °C with the oxygen concentration less than 1%.

2.7. Cytotoxic assay

The cytotoxicities of ABS, Ag_2S@PEG, and Ag_2S@PEG-ABS were evaluated using Cell-Counting Kit-8 (CCK-8) assay kits (Wuhan Kerui Biotechnology Co., Ltd., Wuhan, China). 100 μL of the mouse colon cancer cell lines CT-26 were placed into 96-well plates (5×10^3 cells each well) and cultured for 24 h under normoxia and hypoxia conditions. Then, the cells were incubated with different dilutions of ABS, Ag_2S@PEG, and Ag_2S@PEG-ABS for another 24 h under normoxia and hypoxia conditions. For the photothermal group (Ag_2S@PEG + Laser and Ag_2S@PEG-ABS + Laser), after 24 h of culture, the laser (1.5 W/cm^2) irradiation was given for 5 min. The medium was discarded after the incubation and 100 μL of fresh medium supplemented 10% CCK-8 reagent was added. After that, the cells were cultured for a further 3 h. Ultimately, a Multiskan FC plate reader (Thermo Fisher Scientific Inc.) was used to measure the absorbance of each well and the cell viability was obtained using the formula:

$$\text{Cell viability} = (OD_{sample} - OD_{blank})/(OD_{control} - OD_{blank}) \times 100\%.$$

Annexin V-fluorescein isothiocyanate/propidium iodide (AV-FITC/PI) staining and flow cytometry were used to detect the apoptosis of the CT-26 cells treated with different experimental conditions under hypoxia. After being cultured for 24 h, CT-26 cells were then incubated with ABS, Ag_2S@PEG and Ag_2S@PEG-ABS for another 24 h under hypoxic conditions. The laser treatments were then given 808 nm laser irradiation for 5 min, and finally the cells were collected and washed with cold phosphate-buffered saline

(PBS). Subsequently, the cells were diluted to 1×10^6 cells/mL and stained with 1× binding buffer containing AV-FITC and PI in the dark at room temperature. In the end, the samples were analyzed by flow cytometry.

2.8. Live/dead cell staining

The CT-26 cells were seeded in confocal dishes and then cultured for 24 h. After that, the cells were incubated with different dilutions of ABS, Ag_2S@PEG, and Ag_2S@PEG-ABS for another 24 h under normoxia and hypoxia conditions. After the laser (1.5 W/cm^2) irradiation was given for 5 min for the photothermal group (Ag_2S@PEG + Laser and Ag_2S@PEG-ABS + Laser), PBS wash was operated once for the cells. Then each well was filled with 100 μL of calcein acetoxymethylester/propidium iodide (AM/PI) detection working solution and the cells were incubated at 37 °C for 45 min in the dark. After the incubation, the staining effect was observed and recorded under a fluorescence microscope (OLYMPUS IX73, Olympus Corporation, Tokyo, Japan).

2.9. Establishment of mice cancer model

Institutional Animal Care and Use Committee of Wuhan University authorized the scheme for constructing xenograft colon tumor model (Approval No.: AF074). Male BALB/c mice (18–22 g) were housed in a specific pathogen-free environment with access to enough standardized food and water. To construct the tumor xenograft model, mouse colon cancer cell lines CT-26 in PBS (1×10^6 cells/mL) were subcutaneously injected.

2.10. NIR-II fluorescence imaging of hypoxia tumor

100 μL of Ag_2S QDs (400 μg/mL) and 100 μL of Ag_2S@PEG-ABS (400 μg/mL) were injected separately to animals bearing colon tumor xenografts ($n = 3$) in the *in vivo* NIR-II fluorescence imaging studies. After injection, whole-body NIR-II fluorescence images were taken using the NIR-II imaging system (Suzhou Yingrui Optics Co., Ltd., Suzhou, China). The mice were euthanized and the imaging signals of major organs and tumor tissues were detected after whole-body imaging.

2.11. In vivo antitumor efficacy and safety evaluation

To evaluate the therapeutic effects of the Ag_2S@PEG-ABS, 20 male BALB/c mice with colon tumors were divided into four groups ($n = 5$) at random when the tumor sizes reached about 100 mm^3. The four treatment groups are as follows: 1) PBS; 2) PBS + Laser; 3) Ag_2S@PEG-ABS; and 4) Ag_2S@PEG-ABS + Laser. These preparations (15 mg/kg) were injected once every two days for a total of seven injections (14 days) via the tail vein. After 6 h of the tail vein administration, the PBS + Laser group and the Ag_2S@PEG-ABS + Laser group were laser irradiated for 10 min. Every two days, the weight and tumor sizes were measured and recorded. The tumor volumes were determined by the width and length of the tumor (volume of tumor = length × width × width × 0.5). Tumor inhibition rate (TIR = (1 − tumor weight in treatment group/tumor weight in control group) × 100%) was also calculated.

As mentioned above, male mice of the four groups were all euthanized at the end of treatment, and their major organs (heart, spleen, lung, liver and kidney) and blood samples were collected for

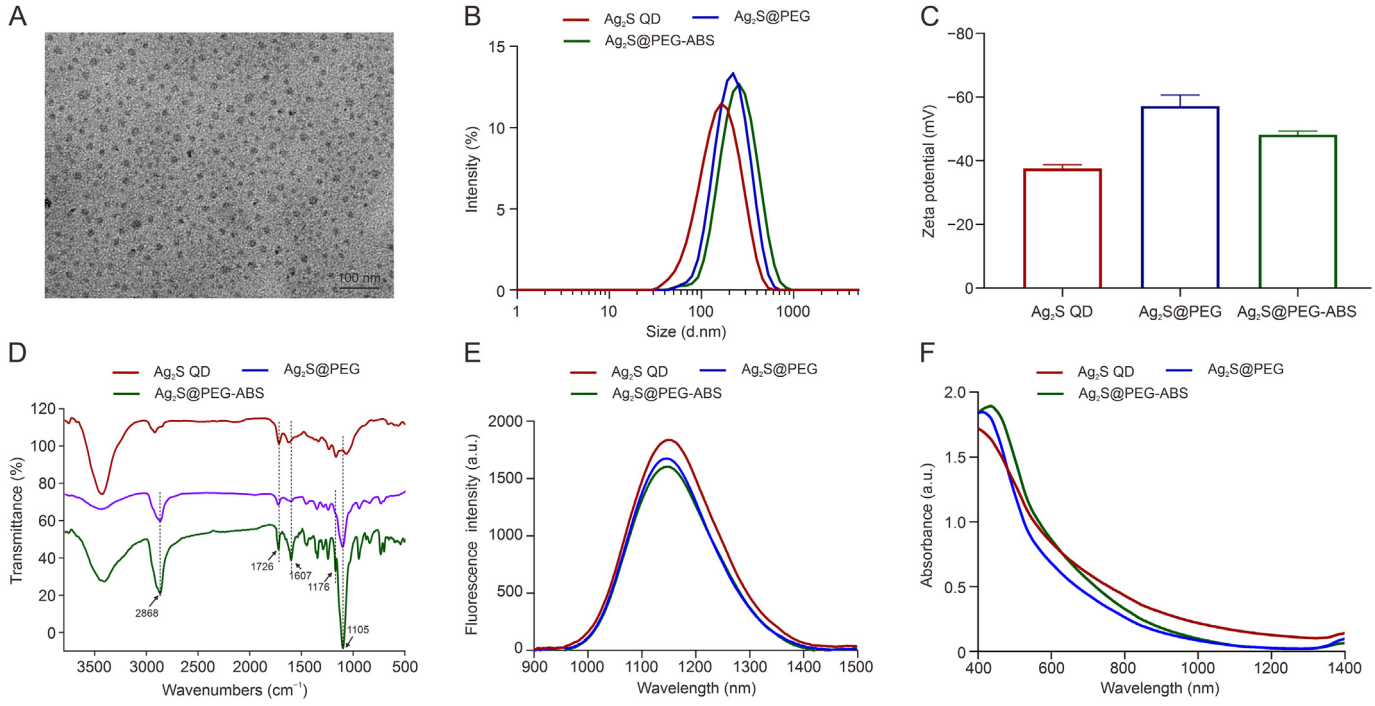

Fig. 1. Characterization of the synthesized products. (A) Transmission electron microscopy (TEM) image of Ag_2S quantum dots (QDs). (B) Hydrodynamic diameter distribution of Ag_2S QDs, Ag_2S@polyethylene glycol (PEG), and Ag_2S@PEG-4-(2-aminoethyl)benzenesulfonamide (ABS) in water measured by dynamic light scattering (DLS). (C) The zeta potential of Ag_2S QDs, Ag_2S@PEG, and Ag_2S@PEG-ABS in an aqueous solution measured by DLS. (D) Fourier transform infrared (FT-IR) spectra of Ag_2S QDs, Ag_2S @PEG, and Ag_2S @PEG-ABS. (E) Fluorescence spectra of Ag_2S QDs, Ag_2S @PEG, and Ag_2S @PEG-ABS in water, respctively ($\lambda_{ex} = 400$ nm and $\lambda_{em} = 1135$ nm). (F) Ultraviolet-visible (UV-vis) absorption spectra of Ag_2S QDs, Ag_2S @PEG, and Ag_2S @PEG-ABS in water.

hematoxylin and eosin (H&E) staining and blood biochemical assessment, including blood urea nitrogen (BUN), alanine transaminase (ALT), aspartate transaminase (AST), creatine kinase (CK), creatinine (Cr), and total bilirubin (T-Bil).

2.12. Statistical analysis

Data were presented as mean ± standard deviation (SD). The statistical analysis was performed with GraphPad Prism 9 software. Statistical differences were determined using one-way analysis of variance (ANOVA), with $P < 0.05$ considered to be statistically significant.

3. Results and discussion

3.1. Synthesis of nanoparticles

PEG modification can improve water solubility and stability. In this work, Ag_2S QDs were modified by ligand exchange method to obtain Ag_2S@PEG. Then, the carboxylic acid group of PEG and amino group in ABS undergo amide condensation reaction to form an amide bond and modify ABS to the surface of Ag_2S@PEG. The size and morphology of the Ag_2S QDs were characterized by TEM. The results of TEM showed that the Ag_2S QDs presented a spherical morphology with a diameter of about 20 nm (Fig. 1A). Dynamic light scattering (DLS) data showed that the average particle sizes of the synthesized Ag_2S QDs were 141.5 nm, while those of Ag_2S@PEG and Ag_2S@PEG-ABS were 188.7 and 229.5 nm, respectively (Fig. 1B). The polydispersity index (PDI) values of Ag_2S@PEG and Ag_2S@PEG-ABS are 0.165 and 0.195, respectively, while the PDI value of Ag_2S QDs is 0.326 (Fig. S2), indicating that the dispersion of Ag_2S@PEG and Ag_2S@PEG-ABS is better than Ag_2S QDs. The zeta potentials of Ag_2S QDs, Ag_2S@PEG, and Ag_2S@PEG-ABS were −37.5, −57.2, and −48.1 mV (Fig. 1C), respectively. Since there are abundant carboxylic acid groups and ether bonds in PEG, the negative charges on the surface of Ag_2S QDs will increase, so the absolute value of negative zeta potential increased after PEG modification. In addition, ether can form hydrogen bonds with water molecules, which also greatly improves the stability and solubility of Ag_2S QDs in water. In the aqueous solution, the nanoparticles with ABS on the surface will adsorb hydrogen ions due to the presence of amino groups, making the surface of the nanoparticles positively charged. Above result of Ag_2S@PEG-ABS showed a change toward a positive zeta potential, which demonstrated the successful modification of ABS. Because the bioprobe has a high negative surface potential, there is a strong electrostatic repulsion between nanoparticles, which is also one of the reasons for the good water solubility after PEG modification. The size and zeta potential of the Ag_2S@PEG-ABS essentially remained unchanged after four weeks of storage, and the water dispersion remained stable (Fig. S3).

The synthesis process of Ag_2S QDs modified by PEG and ABS was further studied by FT-IR spectroscopy (Fig. 1D). In the spectrum, the absorption peaks at 2923 and 2853 cm^{-1} can correspond to the asymmetric and symmetric stretching vibration of −C−H bond in 3-MPA, and the peak at 1726 cm^{-1} is consistent with the stretching vibration of −C═O in carboxylic acid group (−COOH), indicating that the surface ligand 3-MPA is coated on the surface of Ag_2S QDs through Ag−S bond. In the FT-IR spectroscopy of Ag_2S@PEG, the wide peak at 2868 cm^{-1} corresponds to the stretching vibration of −C−H bond of methoxy group in PEG, while the sharp peak at

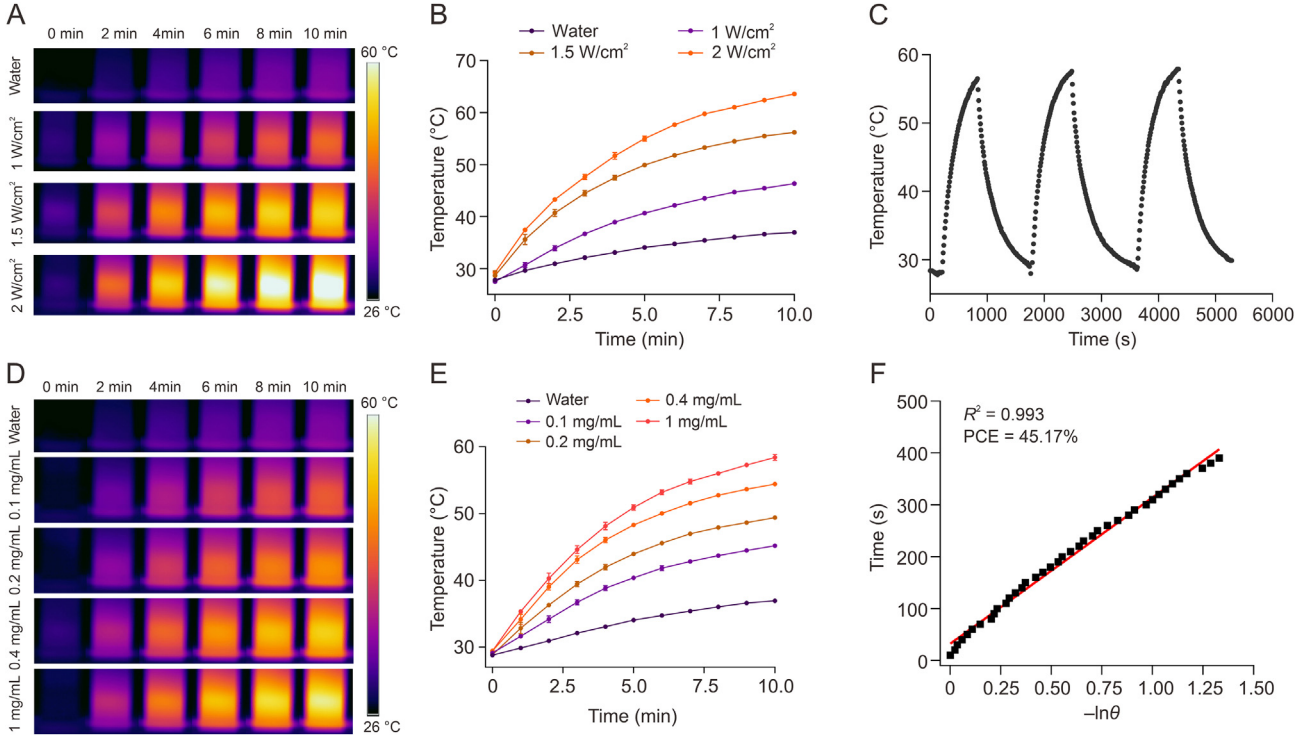

Fig. 2. Photothermal performances of Ag_2S@polyethylene glycol (PEG)-4-(2-aminoethyl)benzenesulfonamide (ABS). (A) Infrared thermal photos of Ag_2S@PEG-ABS in the aqueous solution (0.4 mg/mL) under 808 nm laser irradiation (1, 1.5, and 2 W/cm^2). (B) Temperature change curves of Ag_2S@PEG-ABS (0.4 mg/mL) under 808 nm laser irradiation at different intensities. (C) Temperature variations of Ag_2S@PEG-ABS over three on/off cycles of 808 nm laser irradiation. (D) Infrared thermal photos of Ag_2S@PEG-ABS in the aqueous solution under the laser irradiation (808 nm, 1.5 W/cm^2) at various concentrations. (E) Temperature change curves of Ag_2S@PEG-ABS in the aqueous solution under the laser irradiation (808 nm, 1.5 W/cm^2) at various concentrations. (F) Graph of the time in the cooling period versus the negative natural logarithm of temperature. PCE: photothermal conversion efficiency.

1105 cm^{-1} corresponds to the stretching vibration peak of C—O—C in PEG, indicating that PEG successfully forms a coating on the surface of Ag_2S QDs through ligand exchange. For the final product Ag_2S@PEG-ABS, the peak at 1607 cm^{-1} corresponds to the stretching vibration peak of —C═O in the amide bond, which is greatly enhanced compared with Ag_2S@PEG. In addition, the small peak at 1176 cm^{-1} corresponds to the stretching vibration of —S═O in the sulfonamide, indicating that the amino group in ABS and the carboxylic acid group of the PEG successfully formed the amide bond. As shown in Fig. 1E, the fluorescence emission spectra of Ag_2S QDs, Ag_2S@PEG, and Ag_2S@PEG-ABS did not change significantly, and all of them showed strong fluorescence emission at 1135 nm in the NIR-II. Compared with Ag_2S QDs, the UV-vis spectrum of the Ag_2S@PEG-ABS was enhanced at 400 nm (Fig. 1F), indicating successful modification of ABS. In addition, the bioprobe Ag_2S@PEG-ABS has strong absorption at 808 nm and strong fluorescence emission at 1135 nm, which is conducive to better photothermal performance at 808 nm and imaging in the NIR-II.

The UV absorption and fluorescence emission of the bioprobe at different concentrations were measured. It can be seen that with the increase of concentration, the absorption of the bioprobe at 808 nm gradually increased, and the fluorescence emission intensity also gradually increased (Fig. S4). After that, we tested the effects of different solvents, pH, and ions on the optical properties of the Ag_2S@PEG-ABS (Figs. S5 and S6). The results showed that the fluorescence emission of the bioprobe was the strongest in dimethyl sulfoxide (DMSO) and the fluorescence intensity was the weakest in FBS. The emission spectra were similar between all solvents. Except for DMSO and *N*,*N*-dimethylformamide (DMF), which showed a slight red shift, the Stokes shift of other solvents showed no significant change. In the excitation test of the bioprobe at different pH environments, the enhancement of fluorescence intensity in acidic environment was greater than that in alkaline environment. We measured the fluorescence intensity of the bioprobe in the presence of 50 μM of 10 interfering ions (Fe^{2+}, HPO_4^{2-}, Mn^{2+}, Co^{2+}, Br^-, Cr^{3+}, SO_3^{2-}, SO_4^{2-}, CO_3^{2-}, and Ni^{2+}), and all ions showed no significant quenching (Fig. S6). The above results confirmed that the Ag_2S@PEG-ABS were successfully prepared via ligand exchange and amide condensation reaction and had potential application value in the diagnosis and treatment of hypoxia tumors in the NIR-II region.

3.2. Photothermal performance of Ag_2S@PEG-ABS

PEG modification can significantly improve the water solubility and stability of Ag_2S QDs, and significantly improve the photothermal properties. The photothermal effects of Ag_2S QDs and bioprobe Ag_2S@PEG-ABS were studied under 808 nm laser irradiation. After 5 min laser irradiation, the solution of Ag_2S QDs was

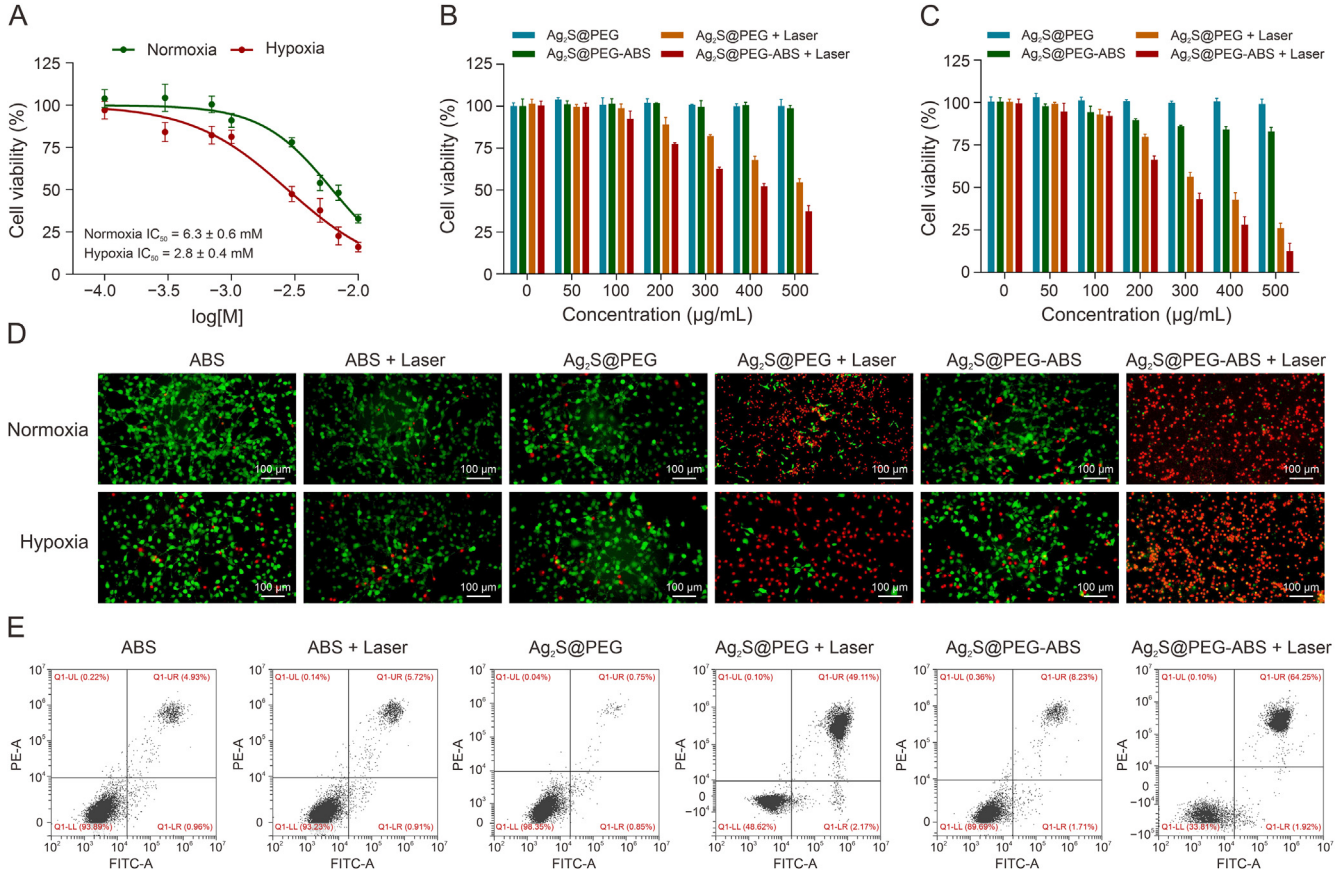

Fig. 3. Antitumor toxicity and photothermal effects of Ag_2S@polyethylene glycol (PEG)-4-(2-aminoethyl)benzenesulfonamide (ABS) *in vitro*. (A) The antitumor toxicity of ABS against CT-26 cells was determined by using Cell-Counting Kit-8 (CCK-8) assay. (B, C) *In vitro* toxicity of Ag_2S@PEG-ABS against CT-26 cells under normoxia (B) and hypoxia (C) conditions. (D) Fluorescence images of CT-26 cells by calcein acetoxymethylester/propidium iodide (calcein AM/PI) staining with different treatments. (E) Effects of different treatments on apoptosis of CT-26 cells under hypoxia conditions were determined by using Annexin V-fluorescein isothiocyanate/propidium iodide (AV-FITC/PI) apoptosis assay. Data are presented as mean ± standard deviation (SD) ($n = 3$). IC_{50}: half maximal inhibitory concentration; PE-A: phycoerythrin area; FITC-A: FITC area; UL: upper left; UR: upper right; LL: lower left ; LR: lower right.

found to settle (Fig. S7), indicating that the light stability of Ag_2S QDs was poor. In contrast, the bioprobe Ag_2S@PEG-ABS exhibits better photothermal properties. Under 808 nm laser irradiation (1.5 W/cm^2), the temperature of the bioprobe aqueous solution at a concentration of 1 mg/mL can rise from 25.8 to 58.8 °C, while the temperature of the water barely changes. At the same concentration, the equilibrium temperature of the bioprobe aqueous solution varies between 44.8 and 61.4 °C after irradiation with different laser power (1, 1.5, and 2 W/cm^2), showing a positive correlation with laser power density (Figs. 2A and B). These results indicate that the PEG-modified Ag_2S QDs improve the photothermal stability, and the bioprobe exhibits highly stable photothermal capacity during the three cycles of laser irradiation (Fig. 2C), while the Ag_2S QDs exhibit relatively poor photostability. In addition, the photothermal effect of the bioprobe is concentration-dependent (Figs. 2D and E). According to the reported method, the PCE of the bioprobe Ag_2S@PEG-ABS was calculated as 45.17% (Fig. 2F). The excellent PCE and light stability of the bioprobe indicated that this bioprobe may be an effective photothermal agent for the treatment of hypoxia tumors.

3.3. *In vitro cytotoxic study of Ag_2S@PEG-ABS*

In order to evaluate the antitumor performance, colon cancer cells CT-26 was selected as the representative of hypoxia tumor cells. The bioprobe has inhibitor ABS, which is conducive to the interaction with CA IX ligand overexpressed on the surface of hypoxia tumor cells. After the interaction of Ag_2S@PEG-ABS with tumor cells, the bioprobe plays the inherent inhibitor role of ABS. Further NIR laser irradiation of the bioprobe can generate local heat, killing tumor cells accurately and efficiently. The IC_{50} value of inhibitor ABS under anaerobic conditions was 2.8 ± 0.4 mM, and that under normal oxygen conditions was 6.3 ± 0.6 mM (Fig. 3A). The results also confirmed that CA IX was overexpressed under hypoxia conditions. The cytotoxicity of the synthesized Ag_2S@PEG and Ag_2S@PEG-ABS was also evaluated by CCK-8 assay. As shown in Figs. 3B and C, the cell survival rate remained almost 100% at Ag_2S@PEG concentrations up to 500 μg/mL under both normal and hypoxia conditions, and the toxicity of Ag_2S@PEG was negligible, suggesting that Ag_2S@PEG had low intrinsic cytotoxicity. Under hypoxia conditions, cell survival rate of Ag_2S@PEG-ABS group was 83.05% at

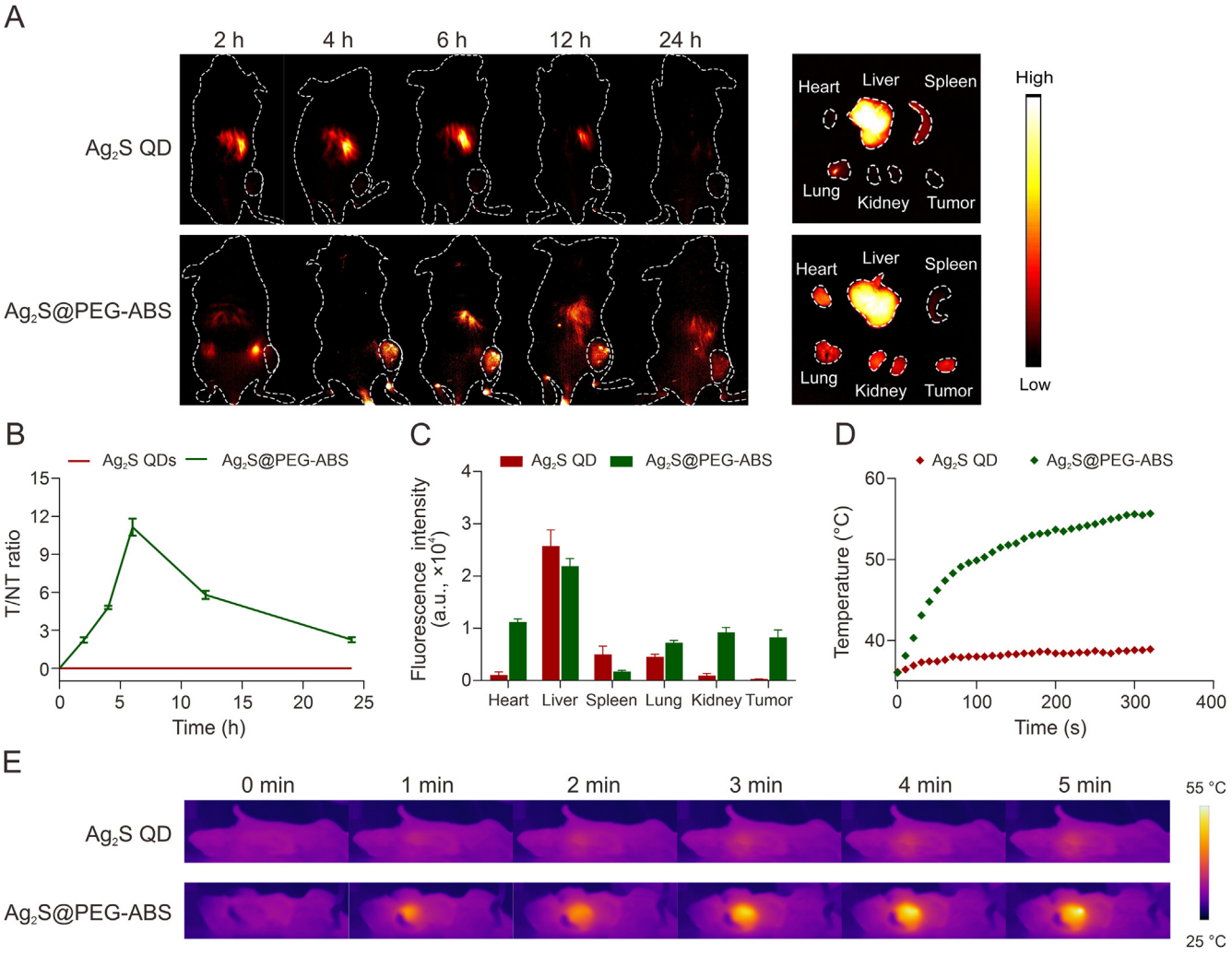

Fig. 4. Near infrared-II (NIR-II) imaging and biodistribution of Ag_2S@polyethylene glycol (PEG)-4-(2-aminoethyl)benzenesulfonamide (ABS) *in vivo*. (A) Whole-body NIR-II imaging results at different time points after the injection of Ag_2S quantum dots (QDs) and Ag_2S@PEG-ABS and fluorescence distribution of major organs and tumors at 24 h after the injection. (B) Corresponding fluorescence intensity ratio between tumor and normal tissue (T/NT) ratio at different time points. (C) Fluorescence intensity of organs and tumors treated with different preparations. (D) Temperature change curves of tumor under the laser irradiation (808 nm, 1.5 W/cm^2). (E) Thermographic images of tumor-bearing mice injected with Ag_2S QDs and Ag_2S@PEG-ABS at different time points.

500 μg/mL, while almost all cells survived at the same concentration of normal oxygen. This also indicated that CA IX was overexpressed on the surface of tumor cells under hypoxia conditions, and the inhibitor ABS of the bioprobe surface played an inherent inhibitory role by specific binding to CA IX. Under normoxia conditions, the IC_{50} of Ag_2S@PEG + Laser group was 547.0 ± 18.9 μg/mL, and that of Ag_2S@PEG-ABS + Laser group was 396.5 ± 10.7 μg/mL (Fig. 3B). However, it is worth noting that the IC_{50} value of the Ag_2S@PEG + Laser group was 340.3 ± 7.4 μg/mL, while that of the Ag_2S@PEG-ABS + Laser group was 263.9 ± 7.1 μg/mL under hypoxia conditions (Fig. 3C). The Ag_2S@PEG-ABS can effectively kill hypoxia tumor cells by utilizing the intrinsic inhibitory activity of ABS and the photothermal properties of Ag_2S QDs. *In vitro* cytotoxicity of the bioprobe was further evaluated by fluorescence analysis of dead and alive cells staining (Fig. 3D). Calcein AM staining showed green fluorescence in living cells and red fluorescence in dead cells stained with PI. As shown in Fig. 3D, when no laser treatment was added, weak cell killing was observed in Ag_2S@PEG groups under both normoxia and hypoxia conditions, indicating that Ag_2S@PEG had great biocompatibility. It is noteworthy that almost all of them showed strong red fluorescence after being irradiated by NIR laser and bioprobe (Ag_2S@PEG-ABS + Laser) under hypoxia conditions, indicating that almost all tumor cells were killed, which verified that Ag_2S@PEG-ABS has good photothermal therapeutic activity. This further confirms that the bioprobe specifically targets hypoxia tumor cells by binding CA IX.

The cells stained with AV-FITC/PI were analyzed by flow cytometry to further examine the apoptosis profiles of the cells treated with different drugs under hypoxia conditions (Fig. 3E). The apoptotic rate showed little difference between ABS incubated cells (4.93%) and ABS incubated cells treated with laser irradiation (5.72%), indicating that the inherent anti-tumor effect of ABS itself was limited, and laser irradiation did not improve its therapeutic effect. The apoptosis rate of the Ag_2S@PEG experimental group was 0.75%, showing that the PEG modified Ag_2S QDs had almost no cytotoxicity and good biocompatibility. The apoptosis rate of the Ag_2S@PEG + Laser experimental group was 49.11%, indicating that the modified Ag_2S QDs had excellent photothermal properties.

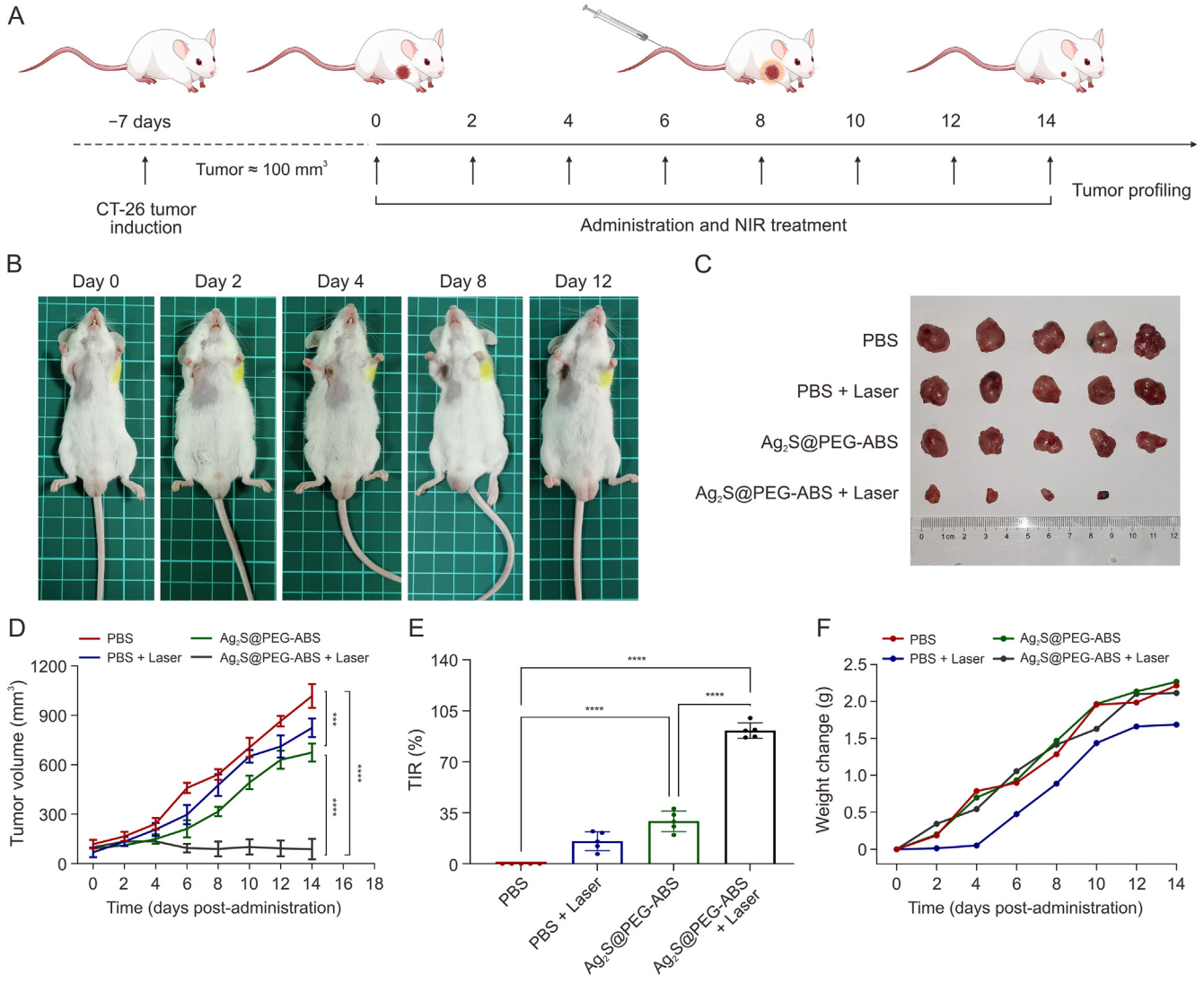

Fig. 5. Evaluation of Ag_2S@polyethylene glycol (PEG)-4-(2-aminoethyl)benzenesulfonamide (ABS) in hypoxia tumors treatment *in vivo*. (A) Schematic illustration of building model of colon tumor-bearing mice and arrangement of treatments. (B) Photographs of the tumor in Ag_2S@PEG-ABS + Laser treatment group on days 0, 2, 4, 8, and 12. (C) Image of the tumors harvested from CT-26 xenograft mice at the end of treatment ($n = 5$). (D) Tumor growth in mice subjected to four different treatments ($n = 5$). (E) Tumor inhibition rate (TIR) of mice with different treatments. (F) Mouse body weights over time following different treatments. Data are presented as mean ± standard deviation (SD) ($n = 3$). Significances are presented by $^{***}P < 0.001$ and $^{****}P < 0.0001$. NIR: near infrared; PBS: phosphate-buffered saline.

There was no significant difference in the apoptosis rate of Ag_2S@PEG-ABS (8.23%) compared with the ABS treatment group. However, it is worth noting that the apoptosis rate of the group incubated with Ag_2S@PEG-ABS and irradiated with laser reached 64.25%, demonstrating that the Ag_2S@PEG-ABS + Laser treatment group had the strongest apoptotic and necrotic ability. These results confirm that Ag_2S@PEG-ABS can target tumor cells through receptor-ligand binding, achieve moderate anti-tumor effect of ABS itself, and play a powerful photothermal killing effect on tumor under NIR laser irradiation. It is further proved that the prepared bioprobe has the synergistic antitumor effect, which can effectively kill tumor cells.

3.4. In vivo imaging of hypoxia tumor

Ag_2S QDs and Ag_2S@PEG-ABS were injected into colon tumor-bearing mice via the tail vein. Whole-body NIR-II fluorescence images of the tumor-bearing mice were collected within 24 h. As

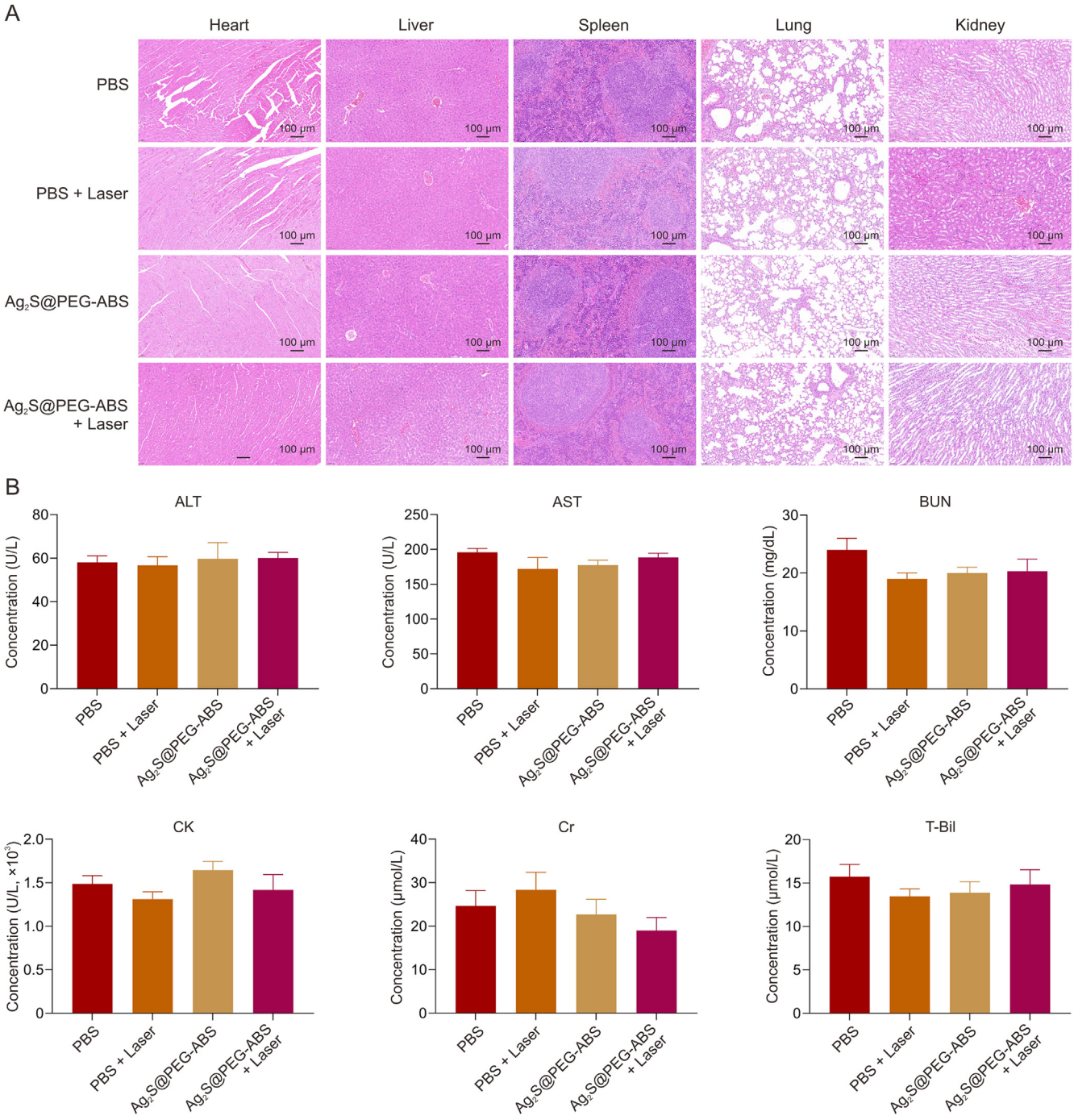

Fig. 6. Histological analysis of major organs and biocompatibility evaluation of Ag_2S@polyethylene glycol (PEG)-4-(2-aminoethyl)benzenesulfonamide (ABS). (A) Hematoxylin and eosin (H&E) staining of the heart, liver, spleen, lung, and kidney in the groups with phosphate-buffered saline (PBS), PBS + Laser, Ag_2S@PEG-ABS, and Ag_2S@PEG-ABS + Laser treatment. (B) Levels of blood biomarkers for hepatic, renal, or cardiac functions in CT-26 xenograft mice following different treatments. ALT: alanine transaminase; AST: aspartate transaminase; BUN: blood urea nitrogen; CK: creatine kinase; Cr: creatinine; T-Bil: total bilirubin.

shown in Fig. 4A, the fluorescence intensity at the tumor site of mice injected with Ag_2S@PEG-ABS increased over time, and the fluorescence intensity reached the maximum at 6 h, while no fluorescence signal was observed at the tumor site of Ag_2S QDs injected mice. Above results showed that the tumor-bearing mice injected with Ag_2S@PEG-ABS have the higher fluorescence intensity in tumors. The ratio of tumor to normal tissue (T/NT) reached the maximum value of 11.2 ± 0.7 at 6 h (Fig. 4B), exceeding the Rose criterion 5 [52]. The T/NT ratio of Ag_2S@PEG-ABS was greater than that of Ag_2S QDs at all-time points, indicating that Ag_2S@PEG-ABS accumulation was enhanced at the tumor site. The mice were euthanized 24 h later, and the main organs and tumors were collected for *in vitro* imaging. The tumors of the Ag_2S@PEG-ABS injected mice exhibited great fluorescence intensity, while those of mice injected with Ag_2S QDs showed no fluorescence signal. Meanwhile, the fluorescence intensity of the liver and spleen was relatively lower in Ag_2S@PEG-ABS group (Figs. 4A and C). This accumulation can be attributed to passively enhanced penetration and retention effects, as well as from the ability of CA IX inhibitors to actively target CA IX ligands. Therefore, we can conclude that the modification of CA IX inhibitor ABS provides active targeting capability to enhance NIR-II tumor imaging of Ag_2S QDs. The temperature of tumor site was measured using an infrared camera while it was being exposed to NIR laser light. The temperature in the Ag_2S@PEG-ABS group could be increased to 55.1 °C (Figs. 4D and E), causing irreversible damage to tumor cells, while the temperature in PBS group was maintained at about 36.2 °C.

3.5. Antitumor efficacy of Ag_2S@PEG-ABS in vivo

As an inherent characteristic of solid tumor, tumor hypoxia is not only one of the important reasons leading to tumor invasion, metastasis, and recurrence, but also inhibits the therapeutic effect of antitumor drugs [53]. To evaluate the therapeutic effect of the bioprobe Ag_2S@PEG-ABS *in vivo*, we constructed the mouse model of colon cancer tumor allograft. Cultured colon CT-26 cells were injected subcutaneously into the right underarm of mice. Mice with colon cancer tumor were randomly divided into PBS group, PBS + Laser group, Ag_2S@PEG-ABS group, and Ag_2S@PEG-ABS + Laser group (Ag_2S@PEG-ABS + Laser group). The drug was injected through the tail vein at days 0, 2, 4, 6, 8, 10, 12, and 14, respectively (Fig. 5A). The laser treatment group was irradiated 6 h after administration, and the weight and tumor size were recorded. The tumor changes of tumor-bearing mice were recorded by taking photographs on the 0, 2, 4, 8, and 12 days. As shown in Fig. 5B, the tumor volume reached about 100 mm^3 on day 0, indicating that the mouse model of colon cancer bearing tumor was successfully established. It can be seen from the photos of the treatment process that after 4 days of treatment, the tumor site of the Ag_2S@PEG-ABS + Laser group was obviously scabbed (Fig. 5B), however there was ineffective inhibition of the tumor in the PBS group. After 14 days of administration, all the tumor-bearing mice were sacrificed and tumors and major organs were extracted. It is noteworthy that the Ag_2S@PEG-ABS + Laser group had the smallest tumor volume (Fig. S8), and with 100% tumor elimination in one case (Fig. 5C). As shown in Fig. 5D, the tumor volume recording data during the treatment period showed that the tumor in the Ag_2S@PEG-ABS + Laser group had already reached the effect of growth inhibition after 6–8 days of treatment, while the tumor in the Ag_2S@PEG-ABS group was still proliferating. In the Ag_2S@PEG-ABS + Laser group, the average tumor inhibition rate was up to 91.5%, while in the Ag_2S@PEG-ABS group, the tumor suppression rate was only 29.2% (Fig. 5E), but the suppression rate was also higher than that in the PBS and PBS + Laser groups. Furthermore, the weight of tumor-bearing mice in different treatment groups increased during treatment period (Fig. 5F), indicating that Ag_2S@PEG-ABS has good biocompatibility. These results showed that Ag_2S@PEG-ABS has an effective synergistic effect of photothermal and intrinsic anti-tumor effect *in vivo*, and can be used for the effective treatment of hypoxia tumor.

3.6. Safety evaluation of Ag_2S@PEG-ABS

After 14 days of treatment, major organs such as heart, liver, spleen, lung, and kidney of tumor-bearing mice in each group were collected, and the biocompatibility of the bioprobe *in vivo* was evaluated by H&E staining. Compared with the two groups treated with PBS, no evident inflammatory lesions and tissue damage were observed in the two groups treated with the Ag_2S@PEG-ABS (Fig. 6A), indicating that the bioprobe has good biocompatibility *in vivo*. Hematological parameters also did not show significant toxicity (Fig. 6B). These results further demonstrate that the bioprobe Ag_2S@PEG-ABS can be used as an effective and safe tumor agent for the diagnosis and treatment of hypoxia tumors.

4. Conclusion

In conclusion, we have successfully synthesized a CA IX targeting bioprobe based on Ag_2S QDs for fluorescence imaging in NIR-II by targeting hypoxia solid tumors and enhanced the therapeutic effect of the tumors through the toxic effect of the inhibitor and the photothermal combination of Ag_2S QDs. In this system, PEG was used to improve the water solubility and colloidal stability of Ag_2S QDs. Ag_2S@PEG-ABS targets the tumor overexpressed CA IX through ligand-receptor interaction and has significant inhibitory effects on CT-26 tumors *in vitro* and *in vivo*. Therefore, this biological probe Ag_2S@PEG-ABS is a new type of integrated probe for the diagnosis and treatment of hypoxic tumors, which can realize the specific diagnosis of hypoxic tumors and then achieve the combination of chemotherapy and photothermal therapy of hypoxic tumors. The preparation method of this Ag_2S@PEG-ABS was quite facile, and the prepared bioprobe possessed outstanding fluorescence imaging and photothermal properties towards hypoxia tumors. This novel bioprobe has a great promising potential for clinical application of hypoxia tumors.

CRediT authorship contribution statement

Xinyue Cui: Investigation, Conceptualization, Methodology, Formal analysis, Data curation, Writing - Original draft preparation; **Zhuang Hu:** Methodology, Formal analysis, Validation; **Ruihan Li:** Validation; **Peng Jiang** and **Yongchang Wei:** Conceptualization, Writing - Reviewing and Editing; **Zilin Chen:** Supervision, Funding acquisition, Project administration, Conceptualization, Writing - Reviewing and Editing.

Declaration of competing interest

The authors declare that there are no conflicts of interest.

Acknowledgments

This work was supported by the National Natural Science Foundation of China (Grant Nos: 82073808 and 82273885).

Appendix A. Supplementary data

Supplementary data to this article can be found online at https://doi.org/10.1016/j.jpha.2024.100969.

References

[1] H. Sung, J. Ferlay, R.L. Siegel, et al., Global cancer statistics 2020: GLOBOCAN estimates of incidence and mortality worldwide for 36 cancers in 185 countries, CA Cancer J. Clin. 71 (2021) 209–249.

[2] N. Keum, E. Giovannucci, Global burden of colorectal cancer: Emerging trends, risk factors and prevention strategies, Nat. Rev. Gastroenterol. Hepatol. 16 (2019) 713–732.

[3] B. Muz, P. de la Puente, F. Azab, et al., The role of hypoxia in cancer progression, angiogenesis, metastasis, and resistance to therapy, Hypoxia (Auckl.) 3 (2015) 83–92.

[4] J. Zhang, L. Li, Stem cell niche: Microenvironment and beyond, J. Biol. Chem. 283 (2008) 9499–9503.

[5] B. Yang, F. Meng, J. Zhang, et al., Engineered drug delivery nanosystems for tumor microenvironment normalization therapy, Nano Today 49 (2023), 101766.

[6] C.T. Supuran, V. Alterio, A. Di Fiore, et al., Inhibition of carbonic anhydrase IX targets primary tumors, metastases, and cancer stem cells: Three for the price of one, Med. Res. Rev. 38 (2018) 1799–1836.

[7] Y. Lou, P.C. McDonald, A. Oloumi, et al., Targeting tumor hypoxia: Suppression of breast tumor growth and metastasis by novel carbonic anhydrase IX inhibitors, Cancer Res. 71 (2011) 3364–3376.

[8] A. Cecchi, A. Hulikova, J. Pastorek, et al., Carbonic anhydrase inhibitors. Design of fluorescent sulfonamides as probes of tumor-associated carbonic anhydrase IX that inhibit isozyme IX-mediated acidification of hypoxic tumors, J. Med. Chem. 48 (2005) 4834–4841.

[9] A. Queen, H.N. Bhutto, M. Yousuf, et al., Carbonic anhydrase IX: A tumor acidification switch in heterogeneity and chemokine regulation, Semin. Cancer Biol. 86 (2022) 899–913.

[10] P. Vermylen, C. Roufosse, A. Burny, et al., Carbonic anhydrase IX antigen differentiates between preneoplastic malignant lesions in non-small cell lung carcinoma, Eur. Respir. J. 14 (1999) 806–811.

[11] A. Janoniene, Z. Liu, L. Baranauskiene, et al., A versatile carbonic anhydrase IX targeting ligand-functionalized porous silicon nanoplatform for dual hypoxia cancer therapy and imaging, ACS Appl. Mater. Interfaces 9 (2017) 13976–13987.

[12] S. Cazzamalli, B. Ziffels, F. Widmayer, et al., Enhanced therapeutic activity of non-internalizing small-molecule-drug conjugates targeting carbonic anhydrase IX in combination with targeted interleukin-2, Clin. Cancer. Res. 24 (2018) 3656–3667.

[13] G. Hong, A.L. Antaris, H. Dai, Near-infrared fluorophores for biomedical imaging, Nat. Biomed. Eng. 1 (2017), 0010.

[14] Y. Yang, Y. Xie, F. Zhang, Second near-infrared window fluorescence nanoprobes for deep-tissue *in vivo* multiplexed bioimaging, Adv. Drug Deliv. Rev. 193 (2023), 114697.

[15] H. Wan, J. Yue, S. Zhu, et al., A bright organic NIR-II nanofluorophore for three-dimensional imaging into biological tissues, Nat. Commun. 9 (2018), 1171.

[16] Y. Fan, F. Zhang, A new generation of NIR-II probes: Lanthanide-based nanocrystals for bioimaging and biosensing, Adv. Opt. Mater. 7 (2019), 1801417.

[17] S. He, J. Song, J. Qu, et al., Crucial breakthrough of second near-infrared biological window fluorophores: Design and synthesis toward multimodal imaging and theranostics, Chem. Soc. Rev. 47 (2018) 4258–4278.

[18] R. Huo, Y. Liu, H. Xu, et al., Associations between carotid atherosclerotic plaque characteristics determined by magnetic resonance imaging and improvement of cognition in patients undergoing carotid endarterectomy, Quant. Imaging Med. Surg. 12 (2022) 2891–2903.

[19] H. Xu, H. Wang, W. Zhao, et al., SUMO1 modification of methyltransferase-like 3 promotes tumor progression via regulating Snail mRNA homeostasis in hepatocellular carcinoma, Theranostics 10 (2020) 5671–5686.

[20] X. Hu, L. Zhou, X. Wu, et al., Review on near-field detection technology in the biomedical field, Adv. Photon. Nexus 2 (2023), 044002.

[21] J.M. Pietryga, R.D. Schaller, D. Werder, et al., Pushing the band gap envelope: Mid-infrared emitting colloidal PbSe quantum dots, J. Am. Chem. Soc. 126 (2004) 11752–11753.

[22] W. Lei, J. Antoszewski, L. Faraone, Progress, challenges, and opportunities for HgCdTe infrared materials and detectors, Appl. Phys. Rev. 2 (2015), 041303.

[23] C. Ding, Y. Huang, Z. Shen, et al., Synthesis and bioapplications of Ag_2S quantum dots with near-infrared fluorescence, Adv. Mater. 33 (2021), 2007768.

[24] B. Purushothaman, J.M. Song, Ag_2S quantum dot theragnostics, Biomater. Sci. 9 (2021) 51–69.

[25] Y. Du, B. Xu, T. Fu, et al., Near-infrared photoluminescent Ag_2S quantum dots from a single source precursor, J. Am. Chem. Soc. 132 (2010) 1470–1471.

[26] P. Awasthi, X. An, J. Xiang, et al., Facile synthesis of noncytotoxic PEGylated dendrimer encapsulated silver sulfide quantum dots for NIR-II biological imaging, Nanoscale 12 (2020) 5678–5684.

[27] S. Qu, Q. Jia, Z. Li, et al., Chiral NIR-II fluorescent Ag_2S quantum dots with stereospecific biological interactions and tumor accumulation behaviors, Sci. Bull. 67 (2022) 1274–1283.

[28] F. Hu, C. Li, Y. Zhang, et al., Real-time *in vivo* visualization of tumor therapy by a near-infrared-II Ag_2S quantum dot-based theranostic nanoplatform, Nano Res. 8 (2015) 1637–1647.

[29] C. Li, X. Yang, J. An, et al., Red blood cell membrane-enveloped O_2 self-supplementing biomimetic nanoparticles for tumor imaging-guided enhanced sonodynamic therapy, Theranostics 10 (2020) 867–879.

[30] D. Zhao, J. Yang, R. Xia, et al., High quantum yield Ag_2S quantum dot@polypeptide-engineered hybrid nanogels for targeted second near-infrared fluorescence/photoacoustic imaging and photothermal therapy, Chem. Commun. (Camb.) 54 (2018) 527–530.

[31] R. Tang, J. Xue, B. Xu, et al., Tunable ultrasmall visible-to-extended near-infrared emitting silver sulfide quantum dots for integrin-targeted cancer imaging, ACS Nano 9 (2015) 220–230.

[32] Z. Wang, Y. Ma, X. Yu, et al., Targeting CXCR4-CXCL12 axis for visualizing, predicting, and inhibiting breast cancer metastasis with theranostic AMD3100-Ag_2S quantum dot probe, Adv. Funct. Mater. 28 (2018), 1800732.

[33] F.D. Duman, M. Erkisa, R. Khodadust, et al., Folic acid-conjugated cationic Ag_2S quantum dots for optical imaging and selective doxorubicin delivery to HeLa cells, Nanomedicine (Lond.) 12 (2017) 2319–2333.

[34] G. Chen, F. Tian, Y. Zhang, et al., Tracking of transplanted human mesenchymal stem cells in living mice using near-infrared Ag_2S quantum dots, Adv. Funct. Mater. 24 (2014) 2481–2488.

[35] E. Sanchez Armengol, A. Unterweger, F. Laffleur, PEGylated drug delivery systems in the pharmaceutical field: Past, present and future perspective, Drug Dev. Ind. Pharm. 48 (2022) 129–139.

[36] S.D. Li, L. Huang, Stealth nanoparticles: High density but sheddable PEG is a key for tumor targeting, J. Control. Release 145 (2010) 178–181.

[37] H. Wang, J. Chang, M. Shi, et al., A dual-targeted organic photothermal agent for enhanced photothermal therapy, Angew. Chem. Int. Ed. Engl. 58 (2019) 1057–1061.

[38] M. Abbas, Q. Zou, S. Li, et al., Self-assembled peptide- and protein-based nanomaterials for antitumor photodynamic and photothermal therapy, Adv. Mater. 29 (2017), 1605021.

[39] J. Lou, A. Heater, G. Zheng, Improving the delivery of drugs and nucleic acids to T cells using nanotechnology, Small Struct. 2 (2021), 2100026.

[40] H. Sun, Q. Zhang, J. Li, et al., Near-infrared photoactivated nanomedicines for photothermal synergistic cancer therapy, Nano Today 37 (2021), 101073.

[41] Y. Zhao, T. Zhao, Y. Cao, et al., Temperature-sensitive lipid-coated carbon nanotubes for synergistic photothermal therapy and gene therapy, ACS Nano 15 (2021) 6517–6529.

[42] D. Zhao, X. Yang, X. Hou, et al., *In situ* aqueous synthesis of genetically engineered polypeptide-capped Ag_2S quantum dots for second near-infrared fluorescence/photoacoustic imaging and photothermal therapy, J. Mater. Chem. B 7 (2019) 2484–2492.

[43] S. Sindhwani, A.M. Syed, J. Ngai, et al., The entry of nanoparticles into solid tumours, Nat. Mater. 19 (2020) 566–575.

[44] M. Landgraf, C.A. Lahr, I. Kaur, et al., Targeted camptothecin delivery via silicon nanoparticles reduces breast cancer metastasis, Biomaterials 240 (2020), 119791.

[45] Z. Hu, R. Li, X. Cui, et al., A pH-sensitive carbonic anhydrase IX-targeted near-infrared probe for fluorescent sensing and imaging of hypoxic osteosarcoma, Sens. Actuat. B Chem. 379 (2023), 133171.

[46] X. Liao, Y. Hong, Z. Chen, Identification and quantification of the bioactive components in *Osmanthus fragrans* roots by HPLC-MS/MS, J. Pharm. Anal. 11 (2021) 299–307.

[47] N. He, Z. Li, C. Hu, et al., *In situ* synthesis of a spherical covalent organic framework as a stationary phase for capillary electrochromatography, J. Pharm. Anal. 12 (2022) 610–616.

[48] Y. Liu, N. He, Y. Lu, et al., A benzenesulfonic acid-modified organic polymer monolithic column with reversed-phase/hydrophilic bifunctional selectivity for capillary electrochromatography, J. Pharm. Anal. 13 (2023) 209–215.

[49] Z. Hu, R. Li, X. Cui, et al., Albumin-based cyanine crizotinib conjugate nanoparticles for NIR-II imaging-guided synergistic chemophototherapy, ACS Appl. Mater. Interfaces 15 (2023) 33890–33902.

[50] Z. Hu, R. Li, X. Cui, et al., Tailoring albumin-based theranostic PROTACs nanoparticles for enhanced NIR-II bioimaging and synergistic cancer chemophototherapy, Chem. Eng. J. 469 (2023), 143883.

[51] P. Jiang, C. Zhu, Z. Zhang, et al., Water-soluble Ag_2S quantum dots for near-infrared fluorescence imaging *in vivo*, Biomaterials 33 (2012) 5130–5135.

[52] A.L. Antaris, H. Chen, K. Cheng, et al., A small-molecule dye for NIR-II imaging, Nat. Mater. 15 (2016) 235–242.

[53] Y. Shao, B. Liu, Z. Di, et al., Engineering of upconverted metal-organic frameworks for near-infrared light-triggered combinational photodynamic/chemo-/immunotherapy against hypoxic tumors, J. Am. Chem. Soc. 142 (2020) 3939–3946.